

Experimental investigation on the turbulence flame autoignition characteristics of ammonia in a high-temperature co-flow

Original

Experimental investigation on the turbulence flame autoignition characteristics of ammonia in a high-temperature co-flow / Ji, M., Wu, Z., Ferrari, A., Vento, O., Shang, Q., Zhang, G., Fu, L., Deng, J., Li, L.. - In: FUEL. - ISSN 0016-2361. - 372:(2024). [10.1016/j.fuel.2024.132216]

Availability:

This version is available at: 11583/2989861 since: 2025-02-05T13:08:56Z

Publisher:

Elsevier

Published

DOI:10.1016/j.fuel.2024.132216

Terms of use:

This article is made available under terms and conditions as specified in the corresponding bibliographic description in the repository

Publisher copyright

Elsevier postprint/Author's Accepted Manuscript

© 2024. This manuscript version is made available under the CC-BY-NC-ND 4.0 license
<http://creativecommons.org/licenses/by-nc-nd/4.0/>. The final authenticated version is available online at:
<http://dx.doi.org/10.1016/j.fuel.2024.132216>

(Article begins on next page)

1 **Experimental investigation on the turbulence flame autoignition characteristics of ammonia**
2 **in a high-temperature co-flow**

3 Meng Ji^{ab}, Zhijun Wu^{a*}, Alessandro Ferrari^{b*}, Oscar Vento^b, Quanbo Shang^a, Guanyu Zhang^a,

4 Lezhong Fu^c, Jun Deng^a, Liguang Li^a

5 a School of Automotive Studies, Tongji University, Shanghai, China

6 b Energy Department, Politecnico di Torino, Turin, Italy

7 c United Automotive Electronic Systems Co., Ltd., Shanghai, China

8 (*) Corresponding Authors

9 **Abstract**

10 Ammonia has a promising future for transportation and industrial power as an innovative zero-
11 carbon fuel because of the harsh emission laws in force and the pressing need of low carbon fuels.
12 Thus, the aim of this work has been to investigate the autoignition characteristics of an ammonia
13 turbulence flame under a high co-flow temperature, on the basis of an experimental platform. The
14 morphology, lift height, and stability of an ammonia jet diffusion flame have been explored under
15 different co-flow regimes (in terms of temperature and velocity) and fuel injection pressures. It was
16 found that when the co-flow temperature augments, the ammonia jet can form a stable lifting flame.
17 Moreover, the combustion stability of the ammonia flame increases significantly and the fluctuation
18 of the lift height of the flame clearly decreases over time. Forming a stable ammonia jet lifting flame
19 under high co-flow velocities and injection pressures requires a high co-flow temperature. The
20 length, area, and perimeter of an ammonia jet diffusion combustion flame increase as the co-flow
21 temperature increases. The distance from the point of autoignition to the central nozzle outlet and
22 the ignition delay both decrease when the co-flow temperature augments. The lift height of an
23 ammonia diffusion combustion flame gradually decreases as the co-flow temperature increases.
24 Moreover, there is a critical temperature of 1173 K beyond which the decline slope of both the lift
25 height and ignition delay decreases.

26
27 **1. Introduction**

28 The traditional internal combustion engine industry is currently in a position where it has to develop
29 clean energies to cope with the increasingly stringent emission regulations of internal combustion
30 engines and to satisfy the zero-carbon policy requirements. The application of and research into

31 zero-carbon fuels have become the main directions for future developments. Ammonia is a new type
32 of low-cost zero-carbon fuel. It can be derived from diverse sources, including traditional fuels such
33 as coal, natural gas, and oil, as well as waste heat, hydropower, urban waste, and various biomass
34 wastes [1]. Ammonia can also be produced from renewable energy sources, such as solar energy,
35 wind energy, geothermal energy and marine energy, for completely carbon-free synthesis [2].
36 Ammonia has been used in industry for more than a century, and its production, storage, and
37 transportation are more complete and mature than other zero-carbon fuels, such as hydrogen.
38 Moreover, because of its relatively mature level of technology, should ammonia be used as a new
39 type of energy in the future, the investment costs will be affordable [3]. Compared with hydrogen,
40 ammonia features valuable storage properties. Indeed, the liquefaction temperature of ammonia is
41 much higher than that of hydrogen, thus opening the way toward the possibility of diminishing the
42 storage pressure. A lower storage pressure and volume could reduce the storage and transportation
43 costs, which are about 10 times and 45 times lower, respectively, than the corresponding ones for
44 hydrogen [4].

45 Back in 1965, General Motors investigated the use of ammonia as a fuel for a single-cylinder spark
46 ignition (SI) engine to free the Armed Forces from reliance on hydrocarbon fuels [5]. Comparing
47 the obtained results with those obtained for gasoline, under similar working conditions, they
48 revealed losses in power and thermal efficiency, due to the inability of the engine to burn ammonia
49 efficiently (as deduced from the large amount of ammonia detected in the exhaust gases). More
50 studies were performed in the mid-60s to assess the compatibility of ammonia with the materials
51 and lubricants used for the manufacturing of internal combustion engines [6], and no serious
52 problems were noted. Different studies have been conducted over the last two decades to explore
53 the applicability of ammonia as a fuel for SI engines, for different compression ratio (CR) values,
54 engine speeds, ammonia amounts and fuel promoters [7-9]. In [10], an SI engine was tested with
55 CR=10.5, and it resulted that the engine could only work under a very low load for a 10% addition
56 of H₂ to promote the ignition of the fuel mixture. On the other hand, the high-octane number (>130)
57 [11] of ammonia helps to improve thermal efficiency, thereby allowing high CR values to be used
58 [12].

59 There are evident difficulties involved in igniting ammonia, due to its high ignition temperature
60 (651 °C) and a narrow ignition range [13]. Furthermore, ammonia may suffer from unstable

61 combustion phenomena, such as misfire and flashback, and these have been ascribed to the low
62 laminar speed of the flame [14]. Despite the abovementioned challenging factors, ammonia also
63 represents a promising fuel for compression ignition (CI) engines, due to their elevated CR, even
64 though the dual-fuel operating condition seems to be the most suitable for light CI engines employed
65 in the transport sector. The impact of replacing diesel fuel with ammonia in an ammonia/diesel dual-
66 fuel engine was studied in [15], and the results showed that up to 84.2% of the input energy can be
67 provided by ammonia. However, since, in this case, the ammonia was injected into the intake port,
68 a reduced compression pressure was reached (the ammonia heat capacity ratio was lower than that
69 of air) and the oxygen concentration in the cylinder diminished (it was difficult for the diesel pilot
70 shot to mix with air and ignite). These two effects, together with the elevated minimum ignition
71 energy of ammonia, led to a delayed start of combustion, compared with that obtainable under a
72 pure diesel working condition.

73 Ammonia-diesel stratified injection was numerically explored for a marine low-speed engine in [16].
74 The diesel fuel, the injection of which occurred before that of the ammonia (both fuels were injected
75 through a dual-fuel DI concentric injector), started to burn because of its short chemical ignition
76 delay: the ammonia close to the combustion area reached an autoignition condition and diffusive
77 combustion started. The results obtained for an injection pressure of 700 bar showed that the ignition
78 delay time in the dual-fuel mode was reduced, compared with the pure diesel working condition,
79 due to the rapid evaporation of ammonia (short physical ignition delay), which contributed to a
80 faster premixing with air, thus reaching a minimum ignition delay value when the diesel energy
81 share was 5%. A CI engine, in which premixed ammonia was used together with an n-heptane pilot
82 shot, was also tested in [17]. Because of its reduced kinematic viscosity, compared with diesel, the
83 addition of n-heptane allowed very small pilot injections and reduced spray droplets to be obtained
84 for the adopted GDI injector (the injection pressure was fixed at 120 bar). It was seen that the
85 ammonia combustion efficiency increased together with the NH_3 fuel energy-share (the latter was
86 varied between 80% and 98.5%). In fact, it was observed that the higher the amount of ammonia of
87 the energy-share was, the lower the local air-to-fuel ratio that approached the stoichiometric value,
88 and the higher the ignition capability of the fuel mixture.

89 The combustion of an ammonia/DME mixture in a CI engine was investigated in [18]. DME was
90 employed to initiate the combustion and, thanks to its polarity, it formed a stable mixture with

91 ammonia; furthermore, since these fuels are characterized by a high vapor pressure, both required
92 pressurization to remain in a liquid state. The results of a direct fuel injection strategy showed that
93 a stable combustion was only achieved for the highest ammonia energy-share (40%) by increasing
94 the fuel injection pressure to 180 bar in order to enhance fuel mixing and atomization, while 150
95 bar was enough for an ammonia energy-share of up to 20%. A higher energy share of ammonia
96 could be reached by increasing the injection pressure [18]; this should not be an issue, considering
97 the elevated injection pressure levels modern diesel Common Rail injection systems [19-22] or GDI
98 ones [23] feature.

99 Many researchers have analyzed the ignition delay [24, 25], flammability limits, and combustion
100 stability of ammonia [26]. Karan explored the laminar flame speed of ammonia at temperatures of
101 300-600 K and under a pressure in the 2-37 bar range, and determined a new set of constants for the
102 evaluation of the laminar flame speed [27]. The experimental results reported in [28] showed that
103 the maximum value of the unstretched laminar burning velocity was below 7 cm/s, that is, lower
104 than those of hydrocarbon flames.

105 Most of the research on ammonia fuel has focused on spherical (laminar) flames [29, 30], and studies
106 on the combustion characteristics of the turbulent jet flame of ammonia fuel at high temperatures
107 has still not been explored in great depth to guide the development of ammonia engines. Some
108 researchers have explored the turbulent flame combustion characteristics of ammonia. In [31], the
109 ammonia turbulent flame propagation speed was measured under oxygen-enriched air conditions,
110 and it was found that lean mixtures were affected more by diffusional instability effects because the
111 mass diffusion of the reactants from the unburned area to the burned one was different from the
112 thermal diffusion from combustion products to reactants (the Lewis number was different from 1).
113 These, together with turbulence eddies, induced a higher turbulent burning velocity. Kobayashi
114 showed that the turbulent methane flame of ammonia resulted in an increased scale of the wrinkled
115 flame front, because of the increased flame thickness of ammonia [32]. In [33], the authors found,
116 by means of direct numerical simulations, that the high heat release rate and NO formation for
117 ammonia/hydrogen blends occurred in correspondence to concave structures of the flame, and lean
118 mixtures showed high turbulent burning velocity values.

119 The experimental research on the autoignition characteristics of an ammonia turbulence jet with a
120 high temperature co-flow and of the subsequent combustion development is essential to explain the

121 diffusive combustion characteristics of ammonia and to support the design of ammonia CI engines.
122 A controlled thermal atmosphere burner (Dibble burner [34,35]) is widely used, and it allows the
123 cause-and-effect relationships between a turbulent flow and chemical reactions to be simplified and
124 investigated. A vitiated co-flow flame is a turbulent flow that reacts within a hot environment, but
125 it has a simplified geometry. A jet of ammonia enters a co-flow of hot combustion products of a
126 lean premixed flame. The large diameter of the co-flow leads the central fuel jet to be isolated from
127 the environment, and the fluid domain may therefore be simplified as a two-stream flow. A wide
128 range of experimental research has been conducted with the Dibble burner on H_2/N_2 [36],
129 H_2/CO_2 [37], $H_2/Ar/O_2$ [38] and methane [39].
130 In this work, ammonia diffusive jet flames have been investigated experimentally in a high-
131 temperature and environment pressure co-flow. The combustion characteristics of the ammonia fuel
132 jet were measured by means of a controlled thermal atmosphere burner. The morphology of the
133 combustion jet flame was examined through an extensive experimental campaign on different co-
134 flow velocities, co-flow temperatures, and ammonia jet velocities. Furthermore, a quantitative
135 analysis was performed concerning the flame stability of a non-premixed ammonia jet and the auto-
136 ignition combustion properties under high temperature conditions, and the influence of the co-flow
137 temperature on both the length of the normalized lift-off and the ignition delay was analyzed. The
138 results of this study can thus be considered as an experimental basis to evaluate and improve
139 combustion models and for the subsequent analysis of ammonia diffusive combustion in a high-
140 pressure and high-temperature co-flow.

141 **2. Experimental design**

142 **2.1 Introduction of the experimental ammonia jet flame combustion device**

143 The test system used for the ammonia fuel combustion experiments is reported in Figure 1, and it is
144 made up of five parts: the main body of the controllable thermal-atmosphere burner, the co-flow
145 control system, the ammonia jet control system, the cooling system, and the data acquisition system.
146 The main element is the controllable thermal-atmosphere burner: it generates a stable co-flow
147 temperature field for ammonia jet combustion. The combustion disk was manufactured with a
148 porous structure. The co-flow premixed gas passes through the porous combustion disk and is
149 ignited above the latter to form countless small premixed laminar flow flames, thus constituting a
150 flat laminar flame that builds a stable high-temperature atmosphere for the jet flame. The porous

151 disk has 874 uniformly distributed 1.2 mm diameter small holes, and the centers of the holes are
152 located 3 mm from each other.

153 The co-flow control system manages both the temperature and the speed of the co-flow field. The
154 former can be varied by acting on the amount of hydrogen in the co-flow, while the latter can be
155 adjusted by means of a blower (cf. Figure 1). The co-flow temperature is measured by means of a
156 thermocouple, and it is used as a feedback signal that acts on the hydrogen pressure reducing value
157 (item 1 in Figure 1) to reach the desired target co-flow temperature value. In order to minimize the
158 interference of the jet combustion on the thermocouple, the latter is arranged at a certain distance
159 from the ammonia injector. The thermocouple was installed on a three-dimensional moving platform
160 to verify the uniformity of the co-flow temperature field, and the temperature was measured at
161 different locations. The temperature is recorder 30 seconds after the thermocouple is moved to allow
162 the thermal regime to be reached. Autoignition occurs for all the considered experimental conditions
163 in the verified uniform part of the co-flow field, which consists of a cylinder with a diameter of
164 around 90 mm and a height of around 180 mm.

165 The co-flow velocity is determined on the basis of the volumetric flowrate of the blower (measured
166 at $T= 20\text{ }^{\circ}\text{C}$ and $p=1\text{ atm}$), and the corresponding mass flowrate can be calculated. The co-flow
167 velocity can then be determined by imposing the mass conservation law, since the burner is exposed
168 to the environment, and by knowing both the burner cross section area (determined on the basis of
169 the diameter of the burner) and the co-flow density, the latter of which is determined by means of
170 the perfect gas law with the measured co-flow temperature (a static pressure equal to 1 atm is
171 considered). The air properties were used to determine the co-flow velocity ($R= 287\text{ J/kgK}$, $\gamma=1.4$)
172 for each set of air volumetric flowrate and co-flow temperature, because of the great excess of the
173 air flowrate compared to the hydrogen one. Figure 2 reports the co-flow velocities for different
174 temperatures and for fixed values of the volumetric flowrates of the blower. As can be inferred from
175 Figure 2, the co-flow velocity is mainly controlled by the flowrate of the blower. However, the co-
176 flow velocity is also a function of the co-flow temperature for a fixed blower flowrate (since the co-
177 flow pressure is fixed, the density reduces when the temperature augments) and such a temperature
178 is increased by augmenting the hydrogen flowrate.

179 The jet control system includes a central injector pipe with an inner diameter, d , of 6.5 mm, an
180 ammonia tank, a solenoid valve, a pressure regulating valve, and a mass flowmeter. The liquid

181 ammonia tank, which is made of stainless steel, is equipped with a pressure gauge with a maximum
 182 pressure of 12 bar. When the ammonia pressure reaches the injection pressure (which is controlled
 183 by means of a device placed between the ammonia tank and the injector), ammonia is in a gas state,
 184 and a solenoid valve, equipped with an LH-04 relay module, opens to start the injection. In order to
 185 realize synchronization between the ammonia injection and the high-speed camera, the LH-04 relay
 186 module was used to control the two signals at the same time, so that the high-speed camera could
 187 receive a 5 V high level signal to begin simultaneously recording with the fuel injection.

188 The cooling system is constituted by two water channels, one for the injection tube (not reported in
 189 Figure 1), and the other for the outer side of the burner. A high-speed camera, which was used to
 190 collect the ammonia fuel combustion experimental data, is included in the data acquisition system.

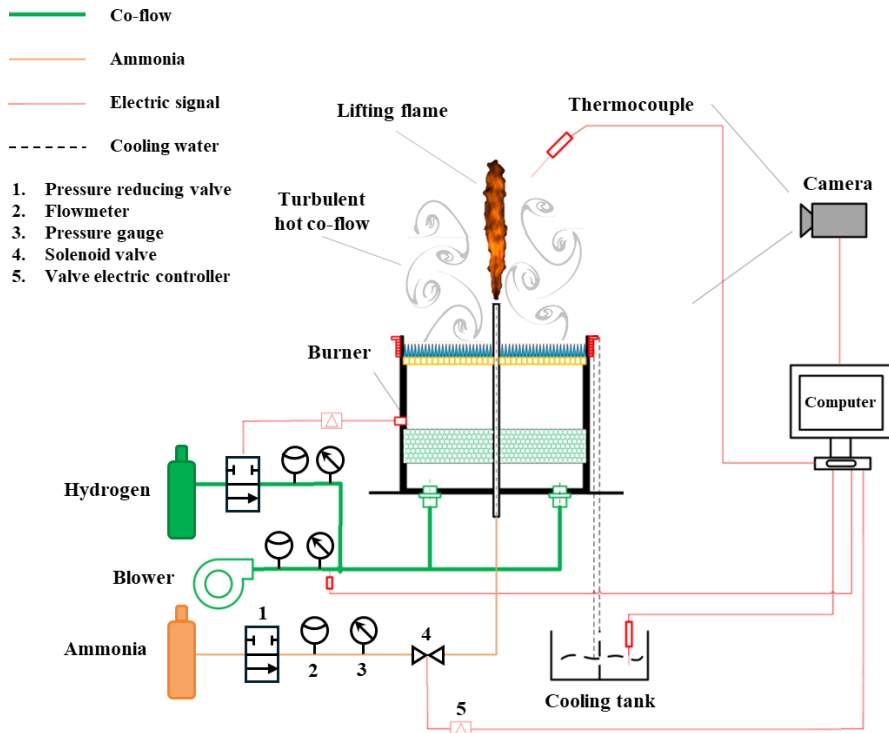
191 Table 1 reports the test conditions in terms of the co-flow velocity (u_{cf}), injection pressure (p_{inj}),
 192 the corresponding injection velocity (u_{inj}), and the co-flow temperature (T_{cf}). The ammonia
 193 pressure range was selected in order to explore the transition from a laminar to turbulent flow regime:
 194 in fact, if $p_{inj} \leq 1.6$ bar, the flow is laminar or in a transitional regime with a Reynolds number
 195 equal to $Re = \rho_{inj} u_{inj} d / \mu_{inj} < 5000$, where $\mu_{inj} = 9.83 \cdot 10^{-6}$ Pa·s is the dynamical viscosity of ammonia and
 196 ρ_{inj} indicates the ammonia density, while the flow is in a turbulent regime ($Re < 15000$) if $p_{inj} \geq 1.9$
 197 bar. The co-flow velocity and temperature values guarantee a turbulent regime ($Re \gg 2000$) for all
 198 the conditions, as usually occurs in the combustion chamber of a CI engine. As can be inferred from
 199 Figure 2, the co-flow temperature only affects the co-flow velocity slightly and is mainly controlled
 200 by the flowrate of the blower. Therefore, for conciseness reasons, in what follows, we refer to a
 201 mean value of the co-flow velocity, averaged over the temperatures, for each blower flowrate (cf.
 202 in Table 1).

203 Table 1. Experimental conditions.

Co-flow velocity (u_{cf}) [m/s]	23, 25, 27, 29, 32, 34
Injection pressure (p_{inj}) [bar]	1.3, 1.6, 1.9, 2.2, 2.5
Injection velocity (u_{inj}) [m/s]	3.6, 10.2, 16.8, 23.4, 29.9
Co-flow temperature (T_{cf}) [K]	1113-1223

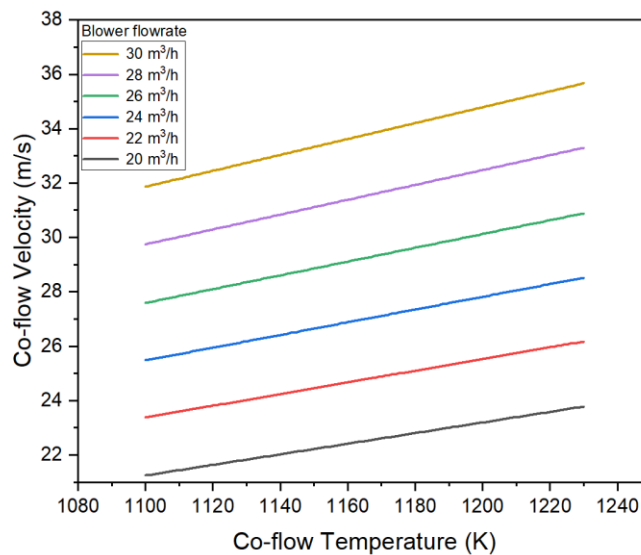
204 As far as the evaluation of u_{inj} is concerned, the presence of a water layer around the fuel pipe
 205 makes the heat transfer from the co-flow to the fuel virtually null during the working conditions of
 206 the burner. The outlet velocity of the fuel jet can be determined by assuming that its temperature is

207 almost equal to the water-cooling temperature. Therefore, the velocity of the ammonia jet was
 208 determined for each tested p_{inj} , on the basis of the measured fuel mass flow-rate, the pipe cross
 209 section area, and the fuel density (the density of the ammonia was calculated under environment
 210 pressure and for the water-cooling temperature).



211
 212

Figure 1. Ammonia fuel combustion test system.



213
 214

Figure 2 Co-flow velocities for different temperatures and blower flowrates.

215 Table 2 reports the compositions of the co-flows, determined by means of CHEMKIN software with
 216 the GRI-Mech 3.0 mechanism [40] and corresponding to the reported T_{cf} values (Y stands for the

217 mass fraction). As can be inferred, when the co-flow temperature increases, the H_2O concentration,
 218 namely Y_{H_2O} , augments slightly, while the nitrogen and oxygen mass fractions reduce slightly (the
 219 Y_{O_2} reduction is around 5% whenever the co-flow temperature passes from 1123 K to 1223 K).

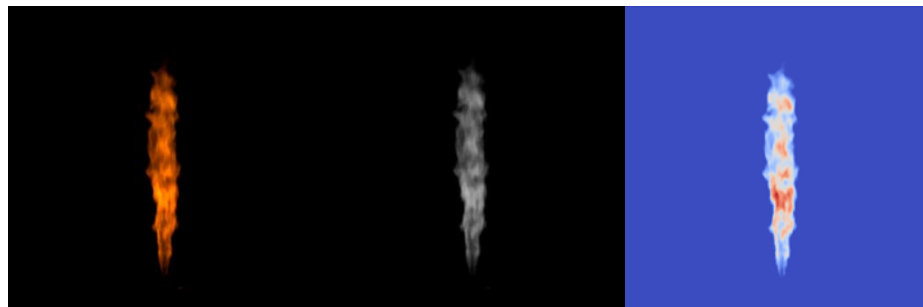
T_{cf}	Y_{H_2O}	Y_{N_2}	Y_{O_2}
1123 K	0.071	0.761	0.168
1148 K	0.074	0.761	0.165
1173 K	0.076	0.76	0.164
1198 K	0.079	0.76	0.161
1223 K	0.081	0.76	0.159

220 Table 2. Co-flow compositions for different co-flow temperatures.

221 2.2 The data processing method

222 The image data extraction program is compiled of Python software to batch-process the flame
 223 images of the turbulent jet of the ammonia fuel under different conditions. The main steps of the
 224 image data extraction algorithm are shown in Figure 3 and can be summarized as follows: the
 225 original flame image is acquired by the camera (cf. Figure 3a); a grayscale flame image (cf. Figure
 226 3b) and a colored flame image (cf. Figure 3c) are obtained; the appropriate threshold for image
 227 binarization (cf. Figure 3d) is obtained by reducing the difference between the morphology of the
 228 original flame picture (Figure 3a) and the one given by the binarization (Figure 3d). Finally, the
 229 contour information and the characteristic parameters, such as the lift height, the flame length, the
 230 flame area, and the perimeter of the flame, are obtained (cf. Fig 3e).

231



232

233

(a) Original figure

(b) Grayscale

(c) Colored grayscale



(d) Binarization (e) Flame data extraction

Figure 3. Data processing method.

234
 235
 236
 237 The extracted characteristic parameters are shown in Figure 4 (the horizontal dashed line represents
 238 the position of the fuel pipe outlet). The normalized flame lift height can be computed by measuring
 239 the distance between the lowest point of the extracted jet flame and the injection outlet, denoted as
 240 H , as the H/d ratio, where d represents the inner diameter of the fuel pipe. The flame length, labeled
 241 L , is defined as the distance between the highest and lowest points of the extracted flame. Moreover,
 242 the flame perimeter is represented by the length, C , of the extracted flame edge. Lastly, the flame
 243 area, denoted as S , is the area enclosed by this edge, and the flame area-to-perimeter ratio is defined
 244 as S/C . Since steady-state flames should be considered, 20-50 consecutive flame pictures with a
 245 visible flame were selected for the experimental analysis, and the average value of each parameter
 246 was calculated as the characteristic parameter of the flame, under certain conditions, to ensure the
 247 reliability of the data. The camera has a resolution of 512×512 pixels, a shooting frequency of 500
 248 Hz, and an exposure time of 2 ms.

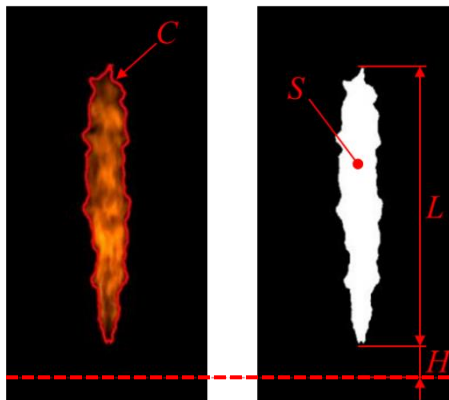


Figure 4. Schematic diagram of the characteristic parameters of the jet flame.

249
 250
 251
 252
 253

254 **3. The diffusion combustion characteristics of ammonia**

255 **3.1 Characteristics of the ammonia jet flame morphology**

256 Figure 5 shows the ammonia diffusion and autoignition process in the co-flow field captured by the
257 high-speed camera under the conditions of $T_{cf} = 1223$ K, $u_{cf} = 25$ m/s, and $p_{inj} = 1.9$ bar. The
258 development process of the jet flame is mainly divided into the following stages: 1) the explosion-
259 proof solenoid valve for the ammonia injection into the high-temperature co-flow field is opened;
260 2) the ammonia jet mixes with air and starts to spontaneously ignite in the high-temperature co-flow
261 field (cf. Figure 5a); 3) and, after autoignition of the ammonia jet, the flame length, flame area, and
262 flame brightness increase rapidly and a stable lifting flame is formed (cf. Figure 5b); 4) after a stable
263 lifting flame of the ammonia jet forms, the flame lasts for a period of time that is mainly determined
264 by the pulse width of the solenoid valve of the ammonia jet; 5) at the end of the ammonia injection,
265 the amount of residual fuel quickly diminishes, and the jet flame is gradually extinguished until the
266 leftover fuel is completely burned (cf. Figure 5c). The considered definition of ignition delay takes
267 into account the time interval between the opening of the solenoid valve, which leads to the start of
268 injection of the ammonia, and the observation of the initial autoignition of the fuel jet.
269 The ammonia jet diffusion flame is orange, in agreement with [41, 42]: the main reason for the
270 formation of this flame is the spectrum of the NH_2 free radicals and water vapor in the ammonia
271 flame. According to the images of the development of the ammonia jet flame and the continuous
272 combustion of the lifting flame taken by the high-speed camera, it can be seen that the ammonia jet
273 presents clear turbulent flame corrugation characteristics.

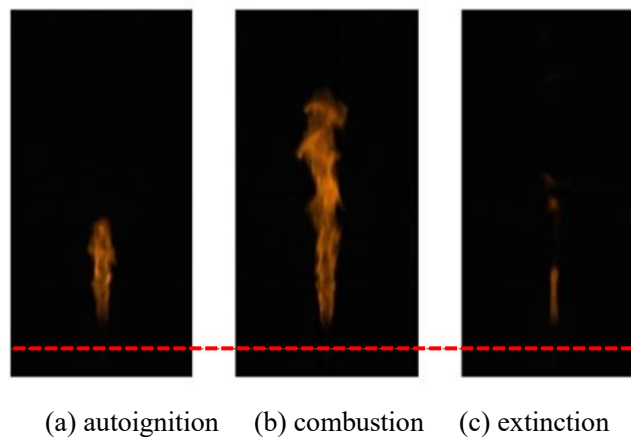
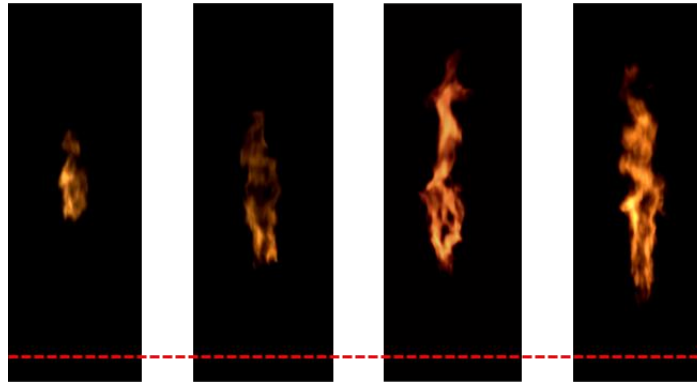


Figure 5. Ammonia diffusion combustion in the co-flow field captured by the high-speed camera.

274 Figure 6a shows the flame characteristics of an ammonia jet, for different T_{cf} , under the conditions

275 of $u_{cf} = 25$ m/s, and $p_{inj} = 1.9$ bar, while Figure 6b reports the brightness of the flame (averaged
276 over the entire flame surface), quantified by means of the R, G, and B values, and the corresponding
277 grayscale value (given by $0.299 \cdot R + 0.587 \cdot G + 0.114 \cdot B$). It can be seen that when the co-flow
278 temperature increases, the ammonia flame becomes lighter and longer, the overall injected ammonia
279 can burn, and combustion becomes more complete and stable. Data referring to a T_{cf} value below
280 1123 K are not reported since the high-speed camera was not able to capture the ammonia jet flame
281 because of its low brightness level. The overall brightness of the flame is low for a T_{cf} value of
282 1148 K, and the length of the flame is also significantly reduced. In this case, the combustion results
283 to be unstable (the flame is sometimes visible and sometimes not), due to the low T_{cf} value. This is
284 evident from Figure 6c, which represents the history of the flame area time during fuel injection: a
285 flame is formed at the beginning for $T_{cf} = 1148$ K, but it is rapidly extinguished. Combustion
286 becomes more stable for higher co-flow temperatures (the sum of the time intervals over which the
287 flame area is higher than zero augments), and the flame can be detected throughout the entire fuel
288 injection time interval for $T_{cf} \geq 1198$ K. When T_{cf} reaches 1223 K, the brightness of the orange flame
289 is significantly enhanced (cf. Figures 6a and 6b), because the high temperature makes the high
290 vibrational excited states of the molecule in the ammonia flame more pronounced. The effects of
291 different co-flow velocities and jet pressures on the stability and characteristic parameters of an
292 ammonia flame were investigated considering the different characteristics of the ammonia flame
293 under different T_{cf} values, and that ammonia cannot form a stable lifting flame under low T_{cf} .
294 Figure 6d shows characteristic images of the ammonia jet flames for different jet velocities under
295 the conditions of $T_{cf} = 1173$ K and a co-flow velocity equal to 25 m/s. It can be seen that the lift
296 height of the flame generally increases as the injection pressure increases. However, when p_{inj}
297 reaches 2.5 bar, the overall brightness of the flame is lower than that at 2.2 bar and the flame length
298 is significantly lower, which indicates that the autoignition of the ammonia jet is unstable. This is
299 due to the large amount of ammonia injected into the co-flow field, which makes the local
300 equivalence ratio become richer. The finite co-flow field limits both the heat exchange and the
301 mixing, thus making it more difficult for ammonia to form a stable flame in such a rich fuel condition.
302 This is why the maximum injection pressure was selected as 2.5 bar.

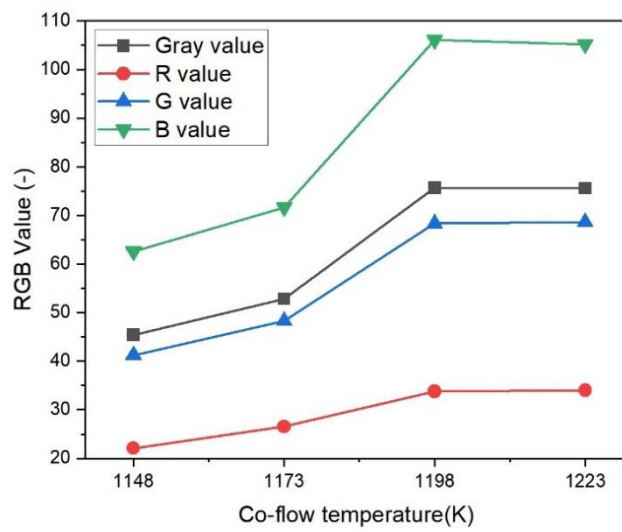


1148 K 1173 K 1198 K 1223 K

303

304

305 a. Pictures of ammonia jet flames for different co-flow temperatures ($u_{cf} = 25$ m/s, $p_{inj} = 1.9$ bar)



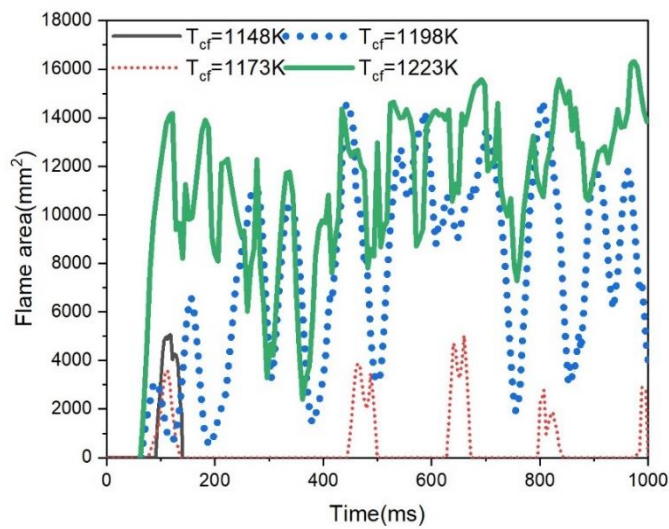
306

307

b. Averaged R, G, B and gray values of an ammonia flame for different co-flow temperatures

308

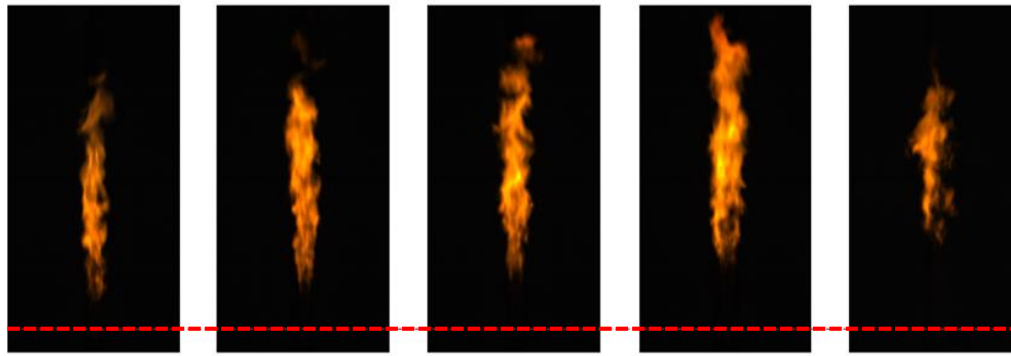
($u_{cf} = 25$ m/s, $p_{inj} = 1.9$ bar)



309

310

c. Time histories of the flame area for different co-flow temperatures ($u_{cf} = 25$ m/s, $p_{inj} = 1.9$ bar)



311

312

1.3 bar

1.6 bar

1.9 bar

2.2 bar

2.5 bar

313

d. Pictures of ammonia jet flames for different injection pressures ($u_{cf} = 25$ m/s, $T_{cf} = 1173$ K).

314

Figure 6. Pictures of the brightness and stability of ammonia jet flames.

315

316 3.2 Study of the autoignition combustion boundary

317

Figure 7 shows the autoignition temperature of ammonia for different co-flow velocities for

318

$p_{inj}=1.9$ bar. Three to five independent experiments were used for each condition to determine the

319

combustion boundary. The blue triangles in Figure 7 represents stable combustion, which means the

320

flame was always observed for those conditions (in terms of u_{cf} and T_{cf}), and the black squares

321

represent the autoignition boundary for each co-flow velocity value, which means that the flame

322

was sometimes recorded (cf. the curve for $T_{cf}= 1173$ K in Figure 6c), while a red circle denotes a

323

condition for which the ammonia jet could not be autoignited. According to the experimental results

324

of the different co-flow velocities reported in Figure 7, the autoignition temperature boundary of the

325

ammonia jet increases as the co-flow speed increases. For example, if we consider a co-flow speed

326

of 23 m/s, it can be seen that the ammonia jet can be autoignited at a co-flow temperature beyond

327

1163 K and form a stable lifting flame. Similarly to Figure 7, Figure 8 shows the autoignition

328

combustion temperature of ammonia for different p_{inj} and for a fixed co-flow velocity equal to 25

329

m/s. According to the experimental results of different jet pressures, the autoignition temperature

330

boundary of the ammonia jet increases as the jet pressure increases. For example, if $p_{inj}=1.6$ bar,

331

the ammonia jet can autoignite when the co-flow temperature is beyond 1158 K and form a stable

332

lifting flame. A higher injection pressure for the same co-flow temperature leads to a higher initial

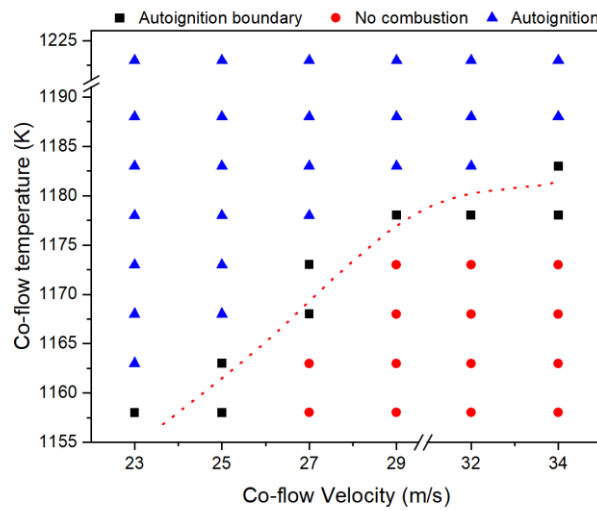
333

momentum and a higher jet velocity. A higher jet velocity reduces both the mixing time between the

334

ammonia and the co-flow and the time available to absorb energy from the co-flow, and the ammonia

335 therefore cannot reach the autoignition temperature. The dashed lines in Figures 7 and 8 denote the
 336 boundaries of the co-flow temperature above which autoignition can be achieved for each co-flow
 337 velocity and injection pressure, respectively. Experimental tests to determine the autoignition
 338 conditions reported in Figures 7 and 8 have been repeated three times, and coincident results have
 339 been obtained.

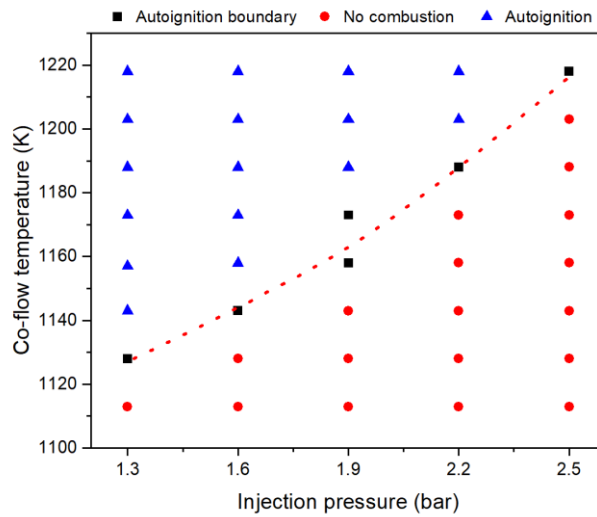


340

341

Figure 7. Autoignition of ammonia for different co-flow velocities ($p_{inj}=1.9$ bar).

342



343

344

Figure 8. Autoignition of ammonia gas for different jet pressures ($u_{cf} = 25$ m/s).

345 3.3 Characteristic parameters of the flame

346 The length and area of the flame are reported in Figure 9 for different co-flow temperatures, while
 347 Figure 10 shows the corresponding perimeter and aspect ratio, S/C , of the flame. In both figures,
 348 u_{cf} has been kept constant at 25 m/s, and p_{inj} is equal to 1.9 bar. Data concerning two different

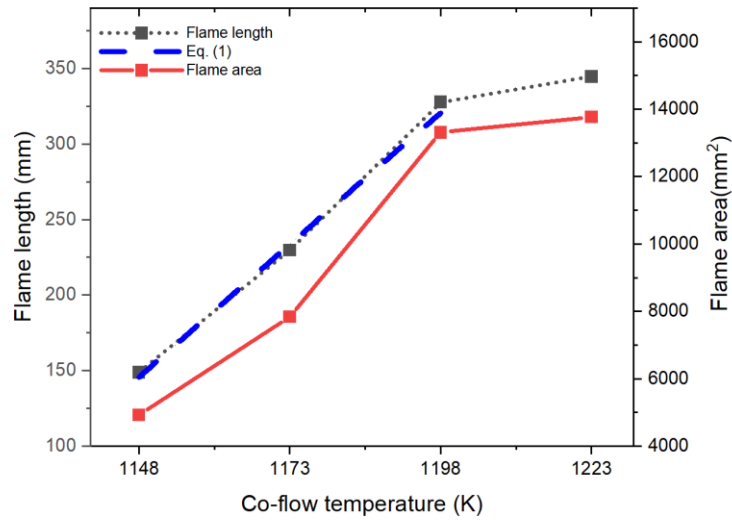
349 acquisitions have been reported, showing a satisfactorily repeatability. As can be inferred from
350 Figures 9 and 10, the length, area, perimeter, and aspect ratio of the ammonia flame increase as T_{cf}
351 increase. The length of the ammonia combustion flame is primarily affected by the flame speed of
352 ammonia. If T_{cf} is increased, the flame speed of ammonia augments [43], thus promoting a faster
353 development of the ammonia flame in the axial direction. Therefore, the diffusion ability of
354 ammonia becomes stronger for an increment of the T_{cf} value, and this leads to an augmented flame
355 area. The flame perimeter also increases together with the value of T_{cf} , due to the more pronounced
356 flame length and wrinkle.

357 When the flame length is mainly regulated by the initial jet momentum [44], it is positively
358 correlated with the ratio of the jet density (ρ_{inj}) to the co-flow density (ρ_{cf}), according to the
359 following law [38]:

$$360 \quad L \propto \left(\frac{\rho_{inj}}{\rho_{cf}} \right)^{0.5} \quad (1)$$

361 The dashed curve plotted in Figure 9, which is based on Eq. (1), was determined from experimental
362 data of co-flow temperatures of up to 1198 K. Indeed, an asymptotic flame length value exists for a
363 certain value of the initial axial jet momentum, i.e. a fixed fuel flow rate: such a value is reached as
364 the fuel jet is able to absorb enough heat from the co-flow to ensure complete combustion. A knee
365 can be observed to have occurred in Figure 9 when $T_{cf}=1198$ K, and the flame length for $T_{cf}>1198$
366 K starts to be less sensitive to T_{cf} , while any further increment only reduces the lift-off length.

367 As can be inferred from Figures 9 and 10, the geometrical features of the flame augment slightly
368 when the co-flow temperature goes beyond 1198 K: this means that, when $T_{cf}=1198$ K, $u_{cf}=25$ m/s,
369 $p_{inj}=1.9$ bar, the fuel jet is already capable of absorbing the required energy from the co-flow field
370 for a complete combustion process, and only marginal modifications in the flame structure can
371 therefore be recognized for a further increment in the co-flow temperature. This result is in line with
372 other results available in the literature concerning hydrogen-argon mixtures [45] and H₂-O₂ coaxial
373 injections [38]. The slight increment in the geometrical parameters of the flame that can be seen
374 when T_{cf} becomes equal to 1223 K can be ascribed to the reduction in the ignition delay, and the
375 fuel jet therefore reaches the autoignition condition closer to the nozzle outlet (the lift-off length
376 reduces), which in turn leads to a small increment in the flame length (cf. Fig. 5) and, consequently,
377 in the perimeter and the area.

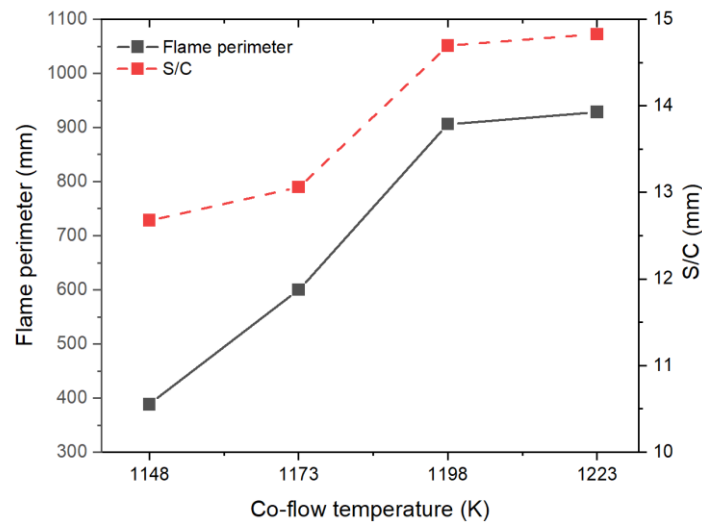


379

380 Figure 9. Flame length, flame length model based on Eq. (1) and flame area of ammonia gas for

381

different co-flow temperatures ($u_{cf} = 25$ m/s, $p_{inj} = 1.9$ bar).



382

383 Figure 10. Perimeter and S/C of the ammonia flame for different co-flow temperatures

384

($u_{cf} = 25$ m/s, $p_{inj} = 1.9$ bar).

385 Figures 11 and 12 compare characteristic parameters of the ammonia jet flame for different injection

386 pressures. The experimental T_{cf} is 1223 K, and the different curves refer to two co-flow velocities

387 equal to 23 m/s (continuous lines) and to 32 m/s (dashed lines). An increase in the co-flow velocity

388 generally augments the turbulence of the co-flow field around the ammonia jet, and it therefore

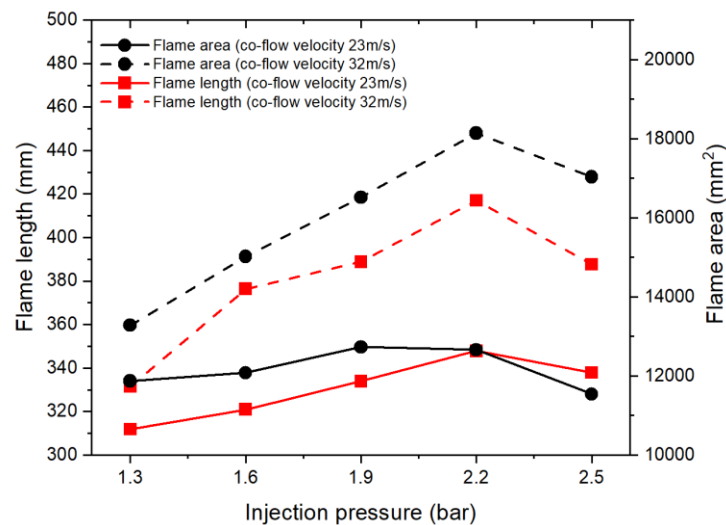
389 promotes heat transfer between the fuel and the co-flow field, thus leading to a growth in the length,

390 the area, the perimeter and in the S/C of the jet flame. The rise in the ammonia jet speed (higher

391 p_{inj}) obviously corresponds to an increment in the volumetric flowrate of ammonia: this enhances

392 the mixing rate with the oxygen that is present in the co-flow, and the temperature of the flame
393 combustion rises, thus improving the diffusion of the ammonia jet gas and promoting chemical
394 reactions. Furthermore, because of the increase in the jet momentum, the diffusion distance of the
395 ammonia jet increases in both the axial and radial directions and leads to a change in the flame
396 morphology.

397 However, when the jet pressure exceeds 2.2 bar, as reported in Figures 11-12, a rapid decline in the
398 length, area, and perimeter of the ammonia flame can be noted. Indeed, a large amount of ammonia
399 is injected into the co-flow field and it cannot be fully burned [46]. Therefore, there may be a large
400 amount of unburned ammonia in the co-flow field, which could lead to a reduction in the length,
401 area, and perimeter of the ammonia flame. However, the perimeter of the flame tends to reduce less
402 than the area and length of the flame for high co-flow velocity values. Indeed, although the length
403 and size of the flame reduce for an elevated co-flow velocity, due to incomplete combustion, the
404 flame can be more wrinkled, due to the elevated u_{cf} , thus mitigating the reduction in the flame
405 perimeter.



406

407 Figure 11. Length and area of the ammonia flame for different jet velocities ($T_{cf} = 1223$ K).

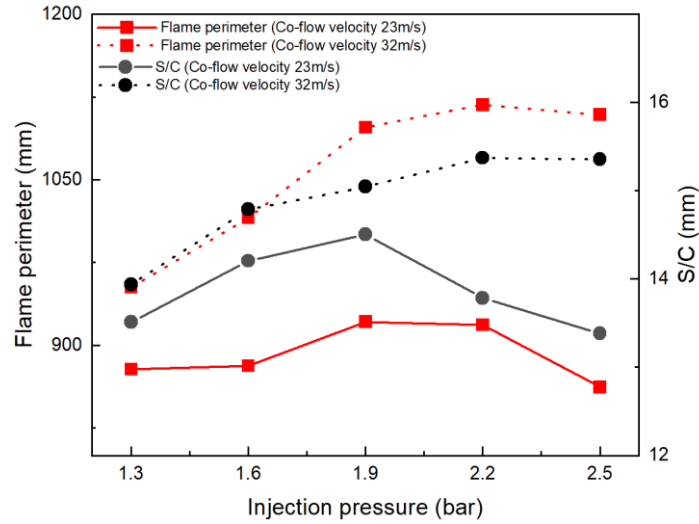


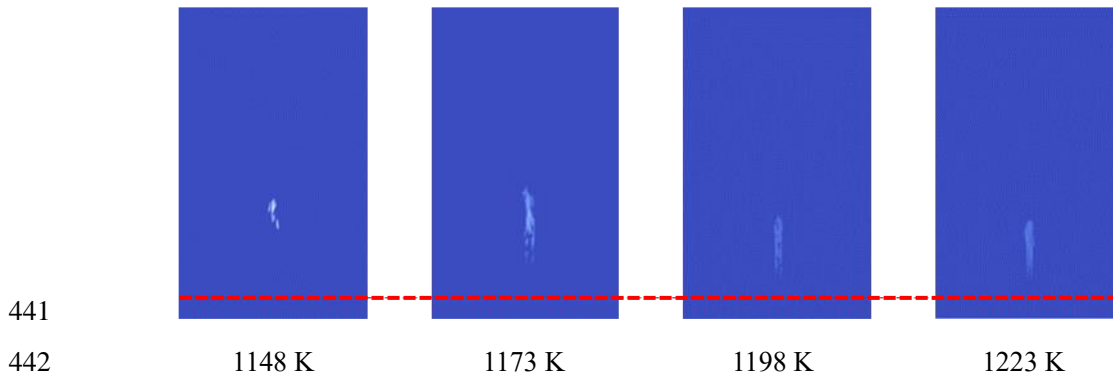
Figure 12. Perimeter and aspect ratio of the ammonia flame for different jet velocities

$$(T_{cf} = 1223 \text{ K}).$$

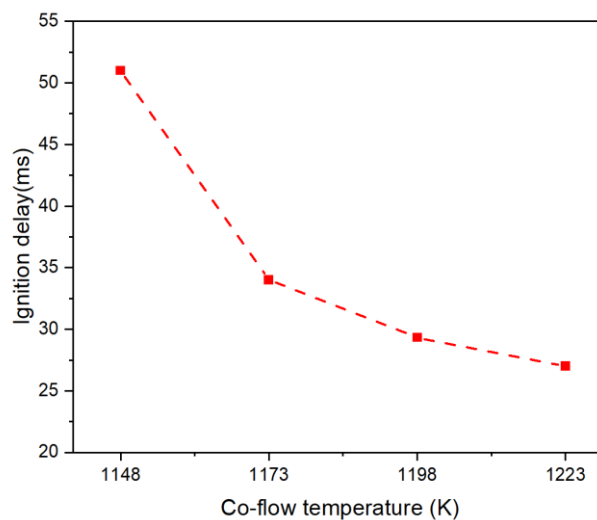
3.4 Autoignition point and ignition delay characteristics of an ammonia flame.

Figure 13 shows the ammonia autoignition location for different co-flow temperature values, considering a co-flow velocity equal to 25 m/s and an injection pressure of 1.9 bar. The autoignition point was assumed as the first flame spot that could be detected by the camera. As can be seen in Figure 13, the position of the autoignition point becomes closer to the nozzle outlet as the co-flow temperature increases. The fire cores from 1148 K to 1173 K are small, scattered and even unconnected, and they show a multi-point distribution accompanied by wrinkles. As the co-flow temperature increases, the fire cores gradually become concentrated, the fuzzy boundary disappears, and the fire core moves closer to the nozzle exit and becomes brighter. Indeed, the augmented co-flow temperature provides the ammonia jet with more energy, thus promoting autoignition and making the position of the autoignition point closer to the nozzle outlet. Figure 14 shows the pattern of the ignition delay with respect to the co-flow temperature for a fixed co-flow velocity and p_{inj} . The reported values, for which a discrepancy below 5% has been observed over three different acquisitions, were determined as intervals between the time instants at which the fuel solenoid valve opened and the first flame that occurred by subtracting the time required for the fuel to flow from the solenoid valve to the pipe outlet at a velocity of $u_{inj} \approx 16.8 \text{ m/s}$ (the distance between the solenoid valve and the fuel pipe outlet was available). The ignition delay of the ammonia jet decreases as T_{cf} increases. When the co-flow temperature is closer to 1148 K, there is still ammonia in the unstable

430 autoignition region (cf. Figure 8), and a rise in the co-flow temperature therefore helps to ensure
 431 combustion stability, which in turn leads to a pronounced drop in the ignition delay to $T_{cf} = 1173$
 432 K. The injection pressure is in fact too high for the tested conditions to allow the ammonia to absorb
 433 enough energy from the co-flow at $T_{cf} = 1148$ K, and this leads to a high value of the flame lift
 434 height and to the presence of unburned ammonia. When T_{cf} rises to 1198 K, the fuel attains a stable
 435 flame lifting, and the ignition delay decreases even further. The energy exchange between the fuel
 436 and the co-flow at this temperature is sufficient to ensure a stable flame. Finally, when the co-flow
 437 temperature exceeds 1198 K, the ammonia flame is always stable, and the influence of the co-flow
 438 temperature on the ignition delay of ammonia is reduced. As mentioned above (cf. Table 2), when
 439 the co-flow temperature changes from 1123 K to 1223 K, the oxygen concentration reduces by about
 440 5%, and its effect on the ignition delay is therefore negligible.



441
 442
 443 Figure 13. Location of the autoignition point of ammonia gas for different co-flow temperatures
 444 ($u_{cf} = 25$ m/s, $p_{inj}=1.9$ bar).

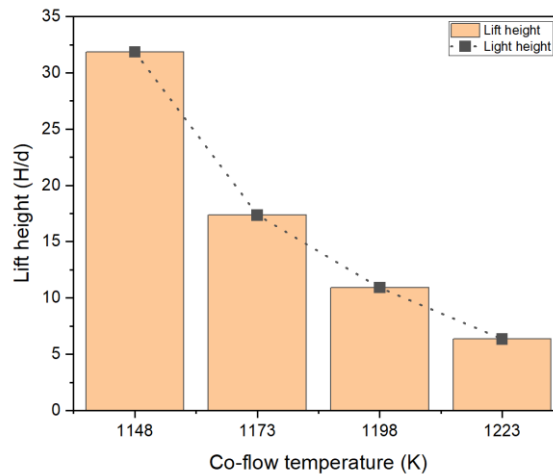


445
 446 Figure 14. Ignition delay period of ammonia gas for different co-flow temperatures
 447 ($u_{cf} = 25$ m/s, $p_{inj}=1.9$ bar).

448 **3.5 Normalized lift height and combustion stability**

449 The normalized flame lift height, H/d , which corresponds to an average position of the flame, can
450 be used to quantify the flame stability since it is sensitive to several flow and flame parameters,
451 especially to the co-flow temperature [35]. Figure 15 compares the H/d of an ammonia jet flame for
452 different co-flow temperatures. The experimental co-flow velocity is equal to 25 m/s, and the
453 injection pressure is 1.9 bar. The normalized lift height of the flame of the ammonia diffusive
454 combustion gradually decreases as the co-flow temperature augments, and the decreasing rate
455 differs significantly for low and high co-flow temperatures. When the co-flow temperature is lower
456 than 1173 K, H/d is particularly sensitive to T_{cf} , whereas the change in the co-flow temperature has
457 less effect for $T_{cf} > 1173$ K. Therefore, the normalized lift height of the flame shows a trend that is
458 very similar to that of the ignition delay (cf. Figure 14). An augmented co-flow temperature even
459 increases the flame stability of H/d , due to an enhanced heat exchange.

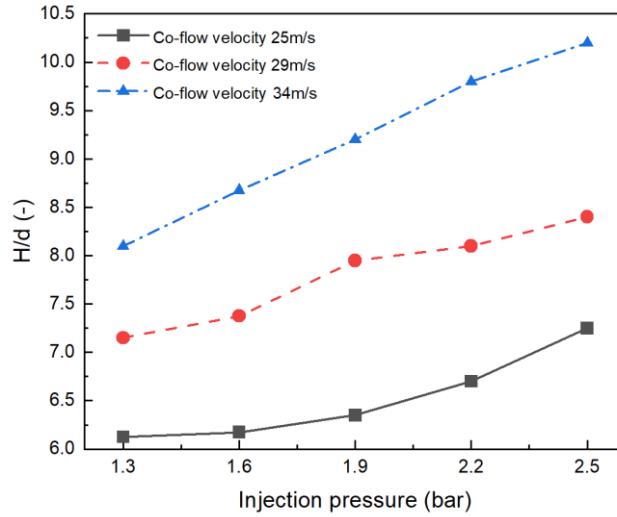
460 By using a controllable thermal atmosphere burner, such as the one employed in this work to study
461 the autoignition of the turbulent flame, it has been shown that many fuels show a co-flow
462 temperature threshold beyond which its influence on the normalized lift height of the flame
463 drastically reduces [47]. The temperature threshold for the ammonia under the considered
464 experimental conditions ($u_{cf} = 25$ m/s, $p_{inj} = 1.9$ bar) can be identified at $T_{cf} = 1173$ K, which
465 corresponds to the knee for both the ignition delay (cf. Figure 14) and the flame H/d (cf. Figure 15).



466
467 Figure 15. Normalized lift height of the ammonia flame for different co-flow temperatures
468 ($u_{cf} = 25$ m/s, $p_{inj} = 1.9$ bar).

469 The velocity and injection pressure of a co-flow have important effects on the normalized lift height
470 of ammonia [48]. Figure 16 compares the H/d trends of the flame with respect to the injection

471 pressure for different co-flow velocities. As already explained, the increase in the ammonia injection
 472 pressure increases the concentration of ammonia in the area near the fuel injection tube, thus leading
 473 to augmented local equivalence ratios, and autoignition is therefore not promoted and the ammonia
 474 flame settles further away from the injector tube outlet.



475

476 Figure 16. Normalized lift height versus injection pressure for different co-flow velocities

477

$$(T_{cf} = 1223 \text{ K}).$$

478 A model for auto-ignited flames in high-velocity co-flows, which is suitable for interpreting the
 479 results in Figures 15 and 16, was developed in [49], where such a model was referred to as “large-
 480 scale mixing model”. In that model, the normalized lift height was expressed as:

481

$$\frac{H}{d} \propto \tau_{ign,ad} \frac{(k_{st})^\alpha}{\tau'_{mix}{}^{1-\alpha}} \quad (2)$$

482

where $\tau_{ign,ad}$ is the ignition delay, determined by means of CHEMKIN, under adiabatic
 483 stoichiometric conditions, k_{st} is the strain rate, α is a parameter in the $[0,1]$ range, and τ'_{mix} is the
 484 mixing time scale of the large eddies. Strain rate k_{st} accounts for the effect of the interaction
 485 between the Kolmogorov eddies, which are the smallest eddies responsible for extinction, and the
 486 flame thickness [50]. When $\alpha = 1$, a small-scale strain has the most important effect on H/d , which
 487 is therefore dominated by the Kolmogorov scale, while large-scale mixing controls the normalized
 488 lift height if $\alpha = 0$. τ'_{mix} considers the effect of large eddies emanated by the fuel jet (the higher the
 489 fuel jet velocity is, the lower τ'_{mix}). These eddies, which are initially only constituted by pure fuel,
 490 then mix with the surrounding air. When the mixture reaches the autoignition condition, a flame
 491 edge is formed and is swept downstream. The air surrounding the flame is heated and becomes
 492 available to ignite the next mixture eddy arriving from the fuel nozzle side. The rapid formation

493 frequency and propagation of eddies allows the flame to remain stable and not to be blown out [51].

494 The flame strain rate in Eq. (2) can be estimated as

495
$$k_{st} \propto \frac{u_{inj}}{d} (Re_{co} \cdot f_M)^{0.5} \quad (3)$$

496 where u_{inj} is the fuel velocity, d is the injector pipe diameter, Re_{co} stands for the Reynolds number

497 of the co-flow, and f_M is defined as

498
$$f_M = \left[1 + \frac{1-M}{\left(\frac{d_{cf}}{d}\right)^2 M} \right]^{0.5} \quad (4)$$

499 In Eq. (4), d_{cf} is the diameter of the burner disk (equal to 100 mm) and M is the specific co-flow-to-

500 jet momentum flux ratio, which is defined as:

501
$$M = \left(\frac{u_{cf}}{u_{inj}} \right)^2 \frac{\rho_{cf}}{\rho_{inj}} \quad (5)$$

502 The large-scale mixing time, τ'_{mix} , in Eq. (2) can be expressed as

503
$$\frac{1}{\tau'_{mix}} \propto \frac{u_{inj}}{L_p} \left[1 + C \left(\frac{\Delta u}{u_{cf}} \right) \right] \quad (6)$$

504 where C is a positive coefficient that represents the degree of the shearing effect on the large-scale

505 mixing time, $\Delta u = u_{inj} - u_{cf}$, and L_p is the potential core length [52], which is evaluated as

506
$$\begin{cases} \frac{L_p}{d} = 4 + 12 \left(\frac{u_{cf}}{u_{inj}} \right) & \text{if } u_{cf} < u_{inj} \\ \frac{L_p}{d} = 16 \cdot \left(\frac{u_{inj}}{u_{cf}} \right) & \text{if } u_{cf} > u_{inj} \end{cases} \quad (7)$$

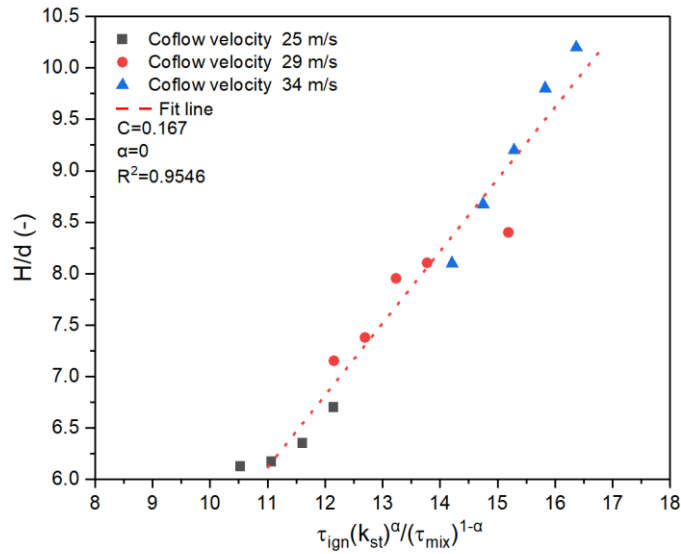
507 The obtained experimental normalized lift height data have been replotted in Figure 17. A

508 satisfactory fit of the dashed-line is found for $C=0.167$ and $\alpha = 0$ when the modified mixing-strain

509 model given by Eq. (2) is used. This means that the diffusive combustion of ammonia is controlled

510 by large-scale mixing in a high-temperature co-flow.

511



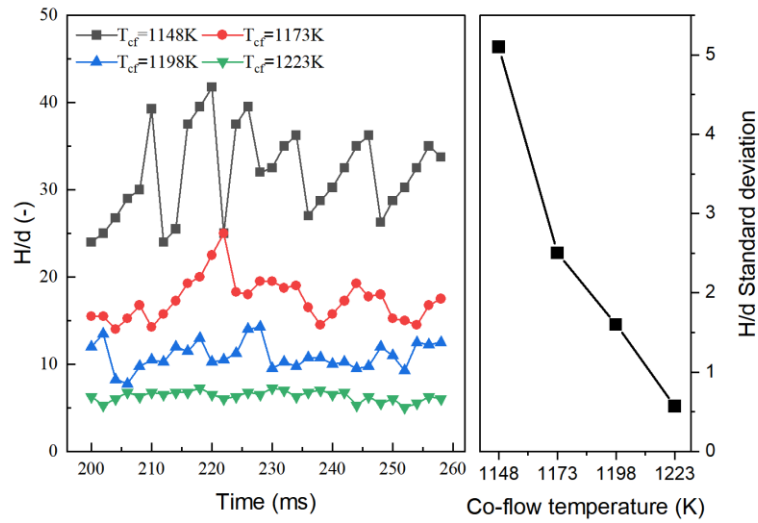
512

513 Figure 17. Modified mixing-strain model correlation of the normalized lift-off height for different
 514 co-flow velocities ($T_{cf}=1223$ K).

515 A measure of the flame stability of the diffusive combustion of ammonia can be obtained from the
 516 time-fluctuations of the flame normalized lift height. Such oscillations are reported in the left part
 517 of Figure 18 for different co-flow temperatures, and for a co-flow velocity and injection pressure
 518 equal to 25 m/s and 1.9 bar, respectively. As the co-flow temperature increases, the flame lift reduces
 519 and becomes more stable. This is also evident in the part on the right of Figure 18, where the standard
 520 deviation of H/d in the considered time interval, i.e. 260ms, is reported: it can be observed that the
 521 standard deviation dramatically reduces when the co-flow temperature increases. The burning flame
 522 diffusion becomes more pronounced for higher co-flow temperatures, because of both the faster
 523 flame speed and lower ignition delay, and the flame stability of ammonia diffusive combustion is
 524 improved. Indeed, when the co-flow temperature is high, the mixing process between the ammonia
 525 in the jet and the oxygen in the co-flow is accelerated, which is more conducive to the formation of
 526 a combustible gas mixture, thus making the combustion become more stable. Moreover, there is no
 527 obvious multi-point autoignition phenomenon.

528 Instead, when the co-flow temperature is low, the combustion of the ammonia jet is somewhat
 529 unstable and is accompanied by a sharp burst sound (this burst sound disappears as soon as the co-
 530 flow temperature exceeds a certain value). The flame front is uneven, the shape is very irregular,
 531 and the direction and speed of the flame front change frequently in the combustion process:
 532 unburned ammonia can be diffused and heated from all directions, and the resulting small explosions

533 emit sharp pressure pulses that cause ringing.



534

535 Figure 18. Normalized lift height time fluctuations for different co-flow temperatures

536

$$(u_{cf} = 25 \text{ m/s}, p_{inj} = 1.9 \text{ bar}).$$

537

The H/d fluctuations, with respect to time, for different injection pressures are reported in Figure 19

538

($u_{cf} = 25 \text{ m/s}$, $T_{cf} = 1223 \text{ K}$). The standard deviation of the normalized lift height of the flame in the

539

considered time interval increases as the injection pressure increases. A higher pressure leads to

540

larger fluctuations, due to the intensified turbulence disturbance caused by the augmented Reynolds

541

number of the fuel. The injection velocity rises as the injection pressure increases, and the flame

542

morphology continuously changes from lift-off to blow-off: the ammonia lifted flame shows a

543

critical autoignition (CA) behavior for $p_{inj} = 2.5 \text{ bar}$, which is represented by continuous flame

544

extinctions and reignitions [53]. It has been verified, on the basis of an analysis of different working

545

conditions, that the stability of the flame can be quantitatively assessed by means of the standard

546

deviation of the normalized lift-off length: as can be inferred from Figures 18 and 19, by considering

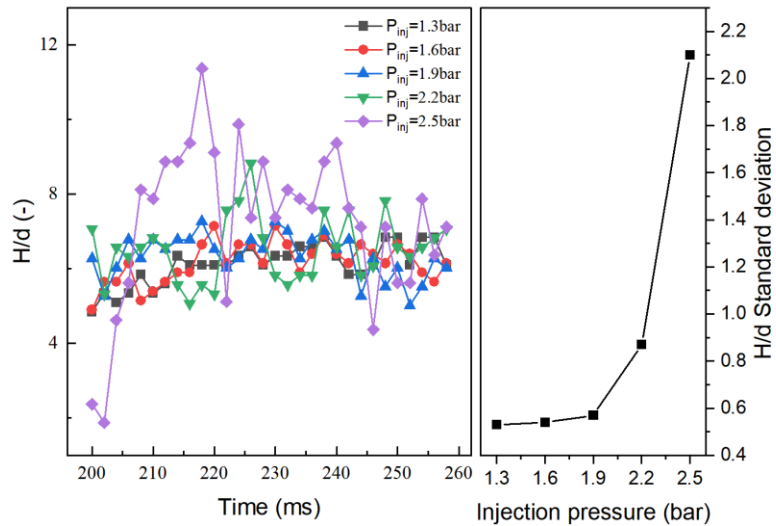
547

the results reported in Figures 7 and 8, when the H/d standard deviation is clearly below 2, the flame

548

can be considered stable.

549



550

551

Figure 19. Normalized lift height time fluctuations for different injection pressures

552

$$(u_{cf} = 25 \text{ m/s}, T_{cf} = 1223 \text{ K}).$$

553

Blow off occurs for ammonia at $p_{inj} = 2.5$ bar and $u_{cf} = 34$ m/s as both the co-flow velocity and

554

injection pressure increase, as reported in Figure 20, where some consecutive flame photos have

555

been reported over the 200-260 ms range after the beginning of the fuel flow: a critical autoignition

556

behavior, featuring the repetition of extinctions and reignition, occurs. The burnt gas could in fact

557

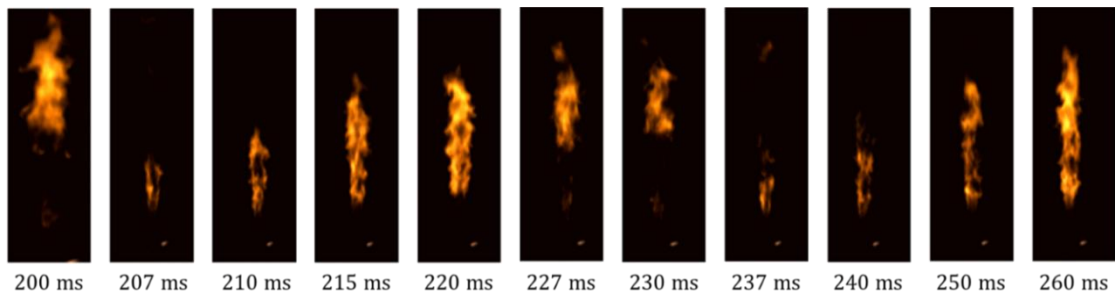
induce a local acceleration in the streamwise velocity, due to buoyancy, and this could lead to a

558

blowout. Autoignition can again occur when the local velocity decelerates, as a result of the

559

mitigation of the buoyancy effect [53].



560

561

Figure 20. Fluctuation and reignition phenomenon of the flame over the 200-260 ms after

562

the beginning of the fuel flow. ($T_{cf} = 1223 \text{ K}$, $p_{inj} = 2.5$ bar, $u_{cf} = 34$ m/s)

563

4. Conclusions

564

The combustion characteristics and flame stability of an ammonia turbulence jet diffusion flame

565

have been investigated for different co-flow temperatures, co-flow velocities, and jet velocities.

566

The ammonia flame appears orange, with sporadic red zones. When $T_{cf} < 1148 \text{ K}$ ($u_{cf} = 25$ m/s,

567

$p_{inj} = 1.9$ bar), a stable lifting flame is not achieved, resulting in low brightness. Extinctions and

568 reignitions are common at $T_{cf}= 1173$ K, and stability increases significantly when $T_{cf}\geq 1198$ K.
569 Increasing co-flow velocity and injection pressure hinders ammonia combustion. Higher co-flow
570 temperature ($T_{cf}> 1223$ K) is necessary for a stable lifting flame at greater co-flow velocity (34 m/s)
571 and injection pressure (2.5 bar).
572 Flame characteristics like length, area, and perimeter increase with co-flow temperature while they
573 first increase and then decrease with the injection pressure. If $sp_{inj} > 2.2$ bar ammonia combustion
574 is incomplete, and flame geometrical characteristics reduce.
575 The distance from the position of the autoignition point to the nozzle outlet and ignition delay both
576 decrease with rising T_{cf} , notably from 1148 K to 1223 K, with the most significant reduction
577 observed at $T_{cf}\leq 1173$ K. Normalized lift height decreases as co-flow temperature rises but, for T_{cf}
578 ≥ 1173 K, the co-flow temperature impact on H/d reduces.
579 The normalized lift-off length data satisfactorily fit a modified mixing-strain model, thus showing
580 that the combustion is controlled by large-scale mixing.
581 Flame stability notably improves with higher co-flow temperatures, evidenced by reduced flame
582 fluctuations over time. A standard deviation of the normalized lift height below 2 indicates a stable
583 flame.

584 **5. Funding**

585 The authors would like to acknowledge the Natural Science Foundation of China [grant numbers
586 T2241003], the Shanghai Science and Technology Program (grant numbers 22ZR1463000) and the
587 Chinese Ministry of Science and Technology (grant numbers G2023133001L) for funding this study.

588 **6. References**

- 589 [1] P.G. Grimes Energy depot fuel production and utilization SAE Trans, 74 (1966), pp. 281-326.
590 [2] D.Richards, R.W. Hender OTEC produced ammonia: an alternative fuel 8th ocean energy
591 conf. (1981), pp. 665-673.
592 [3] T.A. Czuppon, S.A. Knez, J.M. Rovner Ammonia Kirk-othmer encycl. Chem. Technol (fourth
593 ed.), Wiley, New York (1992), pp. 638-691
594 [4] V. Dias, M. Pochet, F. Contino, H. Jeanmart Energy and economic costs of chemical storage
595 Front Mech Eng, 6 (2020), p. 21
596 [5] Cornelius W, Huellmantel L W, Mitchell H R. Ammonia as an engine fuel[J]. SAE Transactions,
597 1966: 300-326

598 [6] Gray Jr J T, Dimitroff E, Meckel N T, et al. Ammonia fuel—engine compatibility and
599 combustion[J]. SAE Transactions, 1967: 785-807.

600 [7] Mørch C S, Bjerre A, Gøttrup M P, et al. Ammonia/hydrogen mixtures in an SI-engine: Engine
601 performance and analysis of a proposed fuel system[J]. Fuel, 2011, 90(2): 854-864.

602 [8] Ge Y T, Fsadni A M, Wang H S. Bubble dissolution in horizontal turbulent bubbly flow in
603 domestic central heating system[J]. Applied energy, 2013, 108: 477-485.

604 [9] Frigo S, Gentili R. Analysis of the behaviour of a 4-stroke Si engine fuelled with ammonia and
605 hydrogen[J]. International Journal of Hydrogen Energy, 2013, 38(3): 1607-1615.

606 [10] Mounaïm-Rousselle C, Bréquigny P, Dumand C, et al. Operating limits for ammonia fuel spark-
607 ignition engine[J]. Energies, 2021, 14(14): 4141.

608 [11] Valera-Medina A, Xiao H, Owen-Jones M, et al. Ammonia for power[J]. Progress in Energy
609 and combustion science, 2018, 69: 63-102.

610 [12] Liu S, Lin Z, Zhang H, et al. Impact of ammonia addition on knock resistance and combustion
611 performance in a gasoline engine with high compression ratio[J]. Energy, 2023, 262: 125458.

612 [13] Hideaki Kobayashi, Akihiro Hayakawa, K.D. Kunkuma A. Somarathne, Ekenechukwu C.
613 Okafor, Science and technology of ammonia combustion, Proceedings of the Combustion
614 Institute, Volume 37, Issue 1, 2019, Pages 109-133,

615 [14] A Valera-Medina, H Xiao, M Owen-Jones, W.I.F. David, P.J. Bowen. Ammonia for power.
616 Progress in Energy and Combustion Science. 2018; 69: 63-102.

617 [15] Ebrahim Nadimi, Grzegorz Przybyła, Michał T. Lewandowski, Wojciech Adamczyk, Effects
618 of ammonia on combustion, emissions, and performance of the ammonia/diesel dual-fuel
619 compression ignition engine, Journal of the Energy Institute, Volume 107, 2023, 101158.

620 [16] Long Liu, Jie Wu, Haifeng Liu, Yue Wu, Yang Wang, Study on marine engine combustion and
621 emissions characteristics under multi-parameter coupling of ammonia-diesel stratified injection
622 mode, International Journal of Hydrogen Energy, Volume 48, Issue 26, 2023, Pages 9881-9894,

623 [17] Niels Førby, Thomas B. Thomsen, Rasmus F. Cordtz, Frantz Bræstrup, Jesper
624 Schramm, Ignition and combustion study of premixed ammonia using GDI pilot injection in CI
625 engine, Fuel, Volume 331, Part 1, 2023, 125768.

626 [18] Gross, Christopher W., and Song-Chang Kong. "Performance characteristics of a compression-
627 ignition engine using direct-injection ammonia–DME mixtures." Fuel 103 (2013): 1069-1079.

628 [19] Ferrari A, Vento O. Thermal effects on Common Rail injection system hydraulic
629 performance[J]. International Journal of Engine Research, 2023: 14680874231162412.

630 [20] Ferrari A, Novara C, Vento O, et al. A novel fuel injected mass feedback-control for single and
631 multiple injections in direct injection systems for CI engines[J]. Fuel, 2023, 334: 126670.

632 [21] Jin Z, Vento O, Zhang T, et al. Numerical-experimental optimization of the common-feeding
633 injection system concept for application to light-duty commercial vehicles[J]. Journal of Energy
634 Resources Technology, 2021, 143(12): 122304.

635 [22] Ferrari, A., Jin, Z., Vento, O., Zhang, T. An injected quantity estimation technique based on
636 time-frequency analysis. Control Engineering Practice 116 (2021): 104910.

637 [23] Ferrari, Alessandro, Pietro Pizzo, and Oscar Vento. "Investigation of a GDI injector with an
638 innovative flowmeter for high-pressure transient flows." International Journal of Engine Research
639 24.9 (2023): 4287-4296.

640 [24] Jun Li, Hongyu Huang, Noriyuki Kobayashi, Chenguang Wang, Haoran Yuan, Numerical study
641 on laminar burning velocity and ignition delay time of ammonia flame with hydrogen addition,
642 Energy, Volume 126, 2017, Pages 796-809.

643 [25] Olivier Mathieu, Eric L. Petersen, Experimental and modeling study on the high-temperature
644 oxidation of Ammonia and related NO_x chemistry, Combustion and Flame, Volume 162, Issue 3,
645 2015, Pages 554-570.

646 [26] Giovanni Battista Ariemma, Giancarlo Sorrentino, Raffaele Ragucci, Mara de Joannon, Pino
647 Sabia, Ammonia/Methane combustion: Stability and NO_x emissions, Combustion and Flame,
648 Volume 241, 2022, 112071.

649 [27] A. Karan, G. Dayma, C. Chauveau, F. Halter Experimental study and numerical validation of
650 oxy-ammonia combustion at elevated temperatures and pressures Combust Flame, 236 (2022),
651 Article 111819.

652 [28] A. Hayakawa, T. Goto, R. Mimoto, Y. Arakawa, T. Kudo, H. Kobayashi Laminar burning
653 velocity and Markstein length of ammonia/air premixed flames at various pressures
654 Fuel, 159 (2015), pp. 98-106.

655 [29] Wu, Zhijun, et al. "Numerical investigation on the flame propagation process of
656 ammonia/hydrogen blends under engine-related conditions." International Journal of Hydrogen
657 Energy 60 (2024): 1041-1053.

658 [30] Hu X, Luo C, Chen X, et al. Study on flame propagation and inherent instability of
659 hydrogen/ammonia/air mixture[J]. Fuel, 2024, 357: 129848.

660 [31] Yu Xia, Genya Hashimoto, Khalid Hadi, Nozomu Hashimoto, Akihiro Hayakawa, Hideaki
661 Kobayashi, Osamu Fujita, Turbulent burning velocity of ammonia/oxygen/nitrogen premixed flame
662 in O₂-enriched air condition, Fuel, Volume 268.

663 [32] H. Kobayashi, A. Hayakawa, K.K.A. Somarathne, E.C. Okafor Science and technology of
664 ammonia combustion Proc Combust Inst, 37 (1) (2019), pp. 109-133

665 [33] Yang W, Dinesh K K J R, Luo K H, et al. Direct numerical simulation of turbulent premixed
666 ammonia and ammonia-hydrogen combustion under engine-relevant conditions[J]. International
667 Journal of Hydrogen Energy, 2022, 47(20): 11083-11100.

668 [34] Ji, Meng, et al. Combustion and Emission Characteristics of Ammonia Jet Flames, Based on a
669 Controllable Activated Thermal Atmosphere. No. 2023-01-1645. SAE Technical Paper, 2023.

670 [35] R. Cabra, J.-Y. Chen, R.W. Dibble, A.N. Karpetis, R.S. Barlow, Lifted methane-air jet flames
671 in a vitiated coflow, Combustion and Flame, Volume 143, Issue 4, 2005, Pages 491-506.

672 [36] Zhang E, Gong Y, Deng J, Hu Z, Jiang C, Wu Z, Li L. Cyclic Variations of Argon Power Cycle
673 Engine with Fuel of Hydrogen. SAE 2017-01-2409.

674 [37] Z. Wu, W. Xie, E. Zhang, et al. Investigation of Flame Characteristics of Hydrogen Jet Issuing
675 into a Hot Vitiated Nitrogen/Argon/Carbon Dioxide Co-flow. International Journal of Hydrogen
676 Energy, 2019, 44(52): 28357-28370.

677 [38] Zhijun Wu, Yang Yu, Wei Xie, Zheng Liu, Liguang Li, Jun Deng, Optimization of the flame
678 characteristics of H₂-O₂ coaxial injection applied to hydrogen-fueled argon cycle engines,
679 International Journal of Hydrogen Energy, Volume 46, Issue 27, 2021, Pages 14780-14789.

680 [39] Qin, Q., Wu, Z., and Ferrari, A. Study on Lifted Flame Stabilization Under Different
681 Background Pressures." ASME. J. Thermal Sci. Eng. Appl. 2022; 14(2): 021006.

682 [40] Gregory P. Smith, David M. Golden, Michael Frenklach, Nigel W. Moriarty, Boris Eiteneer,
683 Mikhail Goldenberg, C. Thomas Bowman, Ronald K. Hanson, Soonho Song, William C. Gardiner,
684 Jr., Vitali V. Lissianski, and Zhiwei Qin http://www.me.berkeley.edu/gri_mech/

685 [41] Akihiro Hayakawa, Takashi Goto, Rentaro Mimoto, Yoshiyuki Arakawa, Taku Kudo, Hideaki
686 Kobayashi, Laminar burning velocity and Markstein length of ammonia/air premixed flames at
687 various pressures, Fuel, Volume 159, 2015, Pages 98-106.

688 [42] Hayakawa A, Goto T, Mimoto R, et al. NO formation/reduction mechanisms of ammonia/air
689 premixed flames at various equivalence ratios and pressures[J]. Mechanical Engineering Journal,
690 2015, 2(1): 14-00402-14-00402.

691 [43] Liang B, Gao W, Zhang K, et al. Ammonia-air combustion and explosion characteristics at
692 elevated temperature and elevated pressure[J]. International Journal of Hydrogen Energy, 2023.

693 [44] Delichatsios M A. Transition from momentum to buoyancy-controlled turbulent jet diffusion
694 flames and flame height relationships[J]. Combustion and Flame, 1993, 92(4): 349-364.

695 [45] Gong Y, Zhan Y, Deng J, et al. Experimental and numerical study on combustion characteristics
696 of hydrogen-argon jet in a hot vitiated Co-flow[R]. SAE Technical Paper, 2018.

697 [46] Choi B C, Kim K N, Chung S H. Autoignited laminar lifted flames of propane in coflow jets
698 with tribrachial edge and mild combustion[J]. Combustion and Flame, 2009, 156(2): 396-404.

699 [47] Wu Z, Bao T, Zhang Q, et al. Experimental study on spray combustion characteristics of
700 gasoline–diesel blended fuel in a controllable active thermo-atmosphere[J]. Fuel, 2014, 135: 374-
701 379.

702 [48] S.R. Turns, R.B. Bandaru, Oxides of Nitrogen Emissions from Turbulent Hydrocarbon/Air Jet
703 Diffusion Flames: Final Report-Phase II, Gas Research Institute, September 1992.

704 [49] Liu G, Li S, Wu Y. Effects of coflow velocity on the lift-off characteristics of autoignited jet
705 flame in hot air coflow[J]. Combustion and Flame, 2024, 259: 113124.

706 [50] Liu G, Li S. Lift-off height of autoignited jet flame in hot air coflow with different O₂
707 contents[J]. Combustion and Flame, 2022, 242: 112144

708 [51] Lawn C J. Lifted flames on fuel jets in co-flowing air[J]. Progress in Energy and Combustion
709 Science, 2009, 35(1): 1-30

710 [52] J. Beér, N. Chigier, Combustion Aerodynamics, Krieger Publishing Company, London, U.K.,
711 1972.

712 [53] Choi, B. C., Chung, S. H. (2010). Autoignited laminar lifted flames of methane, ethylene,
713 ethane, and n-butane jets in coflow air with elevated temperature. Combustion and flame, 157(12),
714 2348-2356.